

Imaging near-fault earthquake deformation with integrated SAR, LiDAR, and Optical Measurements

Craig Glennie
Assoc. Professor
Department of Civil & Environmental Engineering
The University of Houston
cglennie@uh.edu
(832)-842-8861

Final Report: USGS Award G16AC00135
Submitted: April 30, 2020

Project Summary

This project focused on making high precision measurements in the near-field of fault traces that have ruptured in earthquakes or that are creeping continuously. Until recently, this has been a largely unstudied aspect of faulting because of the difficulty in making the near-field measurements. Previous work at UH has examined methodology to determine 3D displacement fields from overlapping temporally spaced point clouds (e.g. (Zhang, Glennie and Kusari 2015a, Glennie et al. 2014)), applying predominantly a technique called iterative closest point (ICP), e.g. (Besl and McKay 1992). The project initially focused on a detailed evaluation of current state of the art techniques, including ICP, and optical image correlation (Leprince et al. 2007) to determine the resolution and accuracy that could be achieved using these methods. Our overall analysis indicated that these current methods were only capable of decimeter level accuracy. We therefore examined point clouds based methods where we used apriori knowledge of the presence of geometric primitives (shapes) in the point data in order to provide additional geometric constraints to the displacement estimate solution. Preliminary results indicate that cm-level displacement estimation may be possible using these constraints. However, significant additional work in automated primitive extraction and matching is required to automate these processes and enable high-resolution and high accuracy estimates of displacement in the near field.

Acknowledgement of Support and Disclaimer

This material is based upon work supported by the U.S. Geological Survey under Grant No. G16AC00135.

The views and conclusions contained in this document are those of the authors and should not be interpreted as representing the opinions or policies of the U.S. Geological Survey. Mention of trade names or commercial products does not constitute their endorsement by the U.S. Geological Survey.

Significant Research Results

Evaluation of Current Optical and 3D Point Cloud Methodologies

The text in this section is a summary of the peer reviewed journal publication pertaining to this work:

Ekhtari, N., and Glennie, C.L., "High-Resolution Mapping of Near-Field Deformation With Airborne Earth Observation Data, a Comparison Study," IEEE Transactions on Geoscience and Remote Sensing, 2018, 56(3), 1598-1614.

We first investigated different approaches that have been presented for estimating near-field surface displacements. Although a number of studies had been undertaken, using different techniques and observations, there had not been a full comparison undertaken on a single earthquake comparing each of these techniques using different input high-resolution remote sensing observations.

We therefore undertook an investigation into different approaches for high-resolution mapping of near-field surface displacement for strike-slip earthquakes. We compared the use of airborne laser scanning (ALS) and high-resolution optical imagery as primary deformation observables. To analyze these sources observations we applied two widely used techniques (1) optical image correlation, using the COSI-Corr algorithm (Leprince et al. 2007) and (2) point cloud differencing techniques using the iterative closest point (ICP) algorithm (Zhang, Glennie and Kusari 2015b). We then compared the performances of these techniques for estimating near-field deformation using pre- and post-event high-resolution ALS and airborne imagery of the August 24, 2014 Mw 6.0 Napa, California earthquake. The dataset was ideal for this purpose as the pre- and post-event datasets both acquired imagery and lidar observations simultaneously, eliminating any possible temporal effects in the comparisons. The estimates of deformation were then compared with field observations of displacement along the fault collected immediately after the earthquake. agree with field observations within a decimeter, at the expected accuracy level of the data.

The results of the analysis are shown in the four figures below, which were extracted directly from the manuscript. The first figure (top left – labeled as Fig. 4) shows the results using optical image correlation (COSI-Corr). While the overall displacement result is accurate at ~decimeter scale in unvegetated areas, the algorithm does not perform well in areas with vegetation (see blue ellipses). Figure 5 below shows that the use of ICP on the ALS point cloud results in a smooth estimate of the displacement. The overall accuracy is at the decimeter level, but there are none of the anomalies due to vegetation, as lidar observations are able to penetrate vegetation to get to the ground underneath. The final analysis, in Figure 6 is a hybrid approach, where the high-resolution imagery is converted to a 3D point cloud using structure from motion software, and then the resultant point cloud is run through the ICP algorithm.

Again, accuracy in unvegetated areas is similar to lidar at the decimeter level, but underperforms in areas of vegetation. A comparison of fault displacement profiles along the rupture, compared with field observations is finally given in Figure 8 below. In general the agreement is confirmed to be at ~decimeter level. Overall, we conclude that ALS data are generally better than imagery for estimating near-field deformation regardless of the estimation methodology and that the iterative closest point algorithm was more effective at recovering the displacement signal. However, given the high-resolution of the data, it seems unlikely that accuracy better than the level observed here would be possible using current ICP techniques.

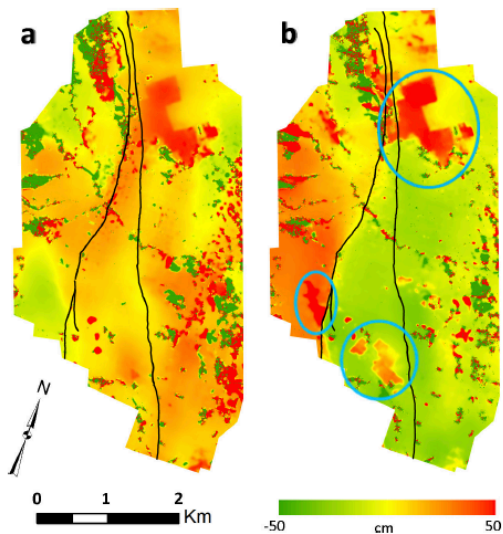


Fig. 4. Horizontal components of displacement field estimated with aerial orthoimages using COSI-Corr. (a) EW component. (b) NS component. Raw displacement estimates have been filtered using the NL-means filter. Black lines depict the field measured fault traces A and C [5], [50]. Blue ellipses mark the location of vineyards over which an artifact in the displacement maps is observed.

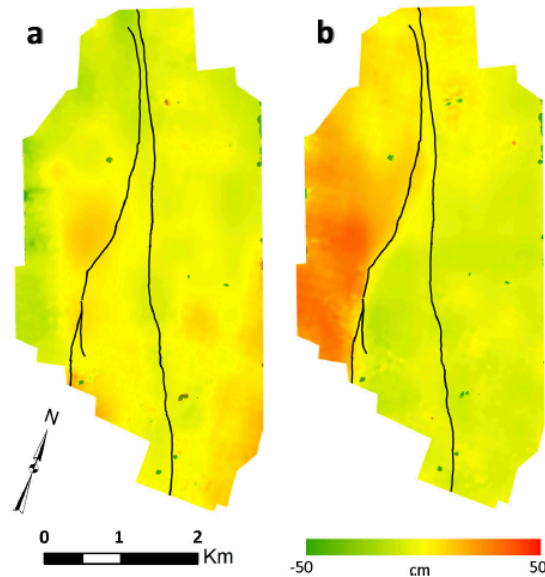


Fig. 5. Horizontal components of displacement field estimated with ALS data using ICP. (a) EW component. (b) NS component. Raw displacement estimates have been filtered using the NL-means filter. Black lines: field measured fault traces A and C [5], [50].

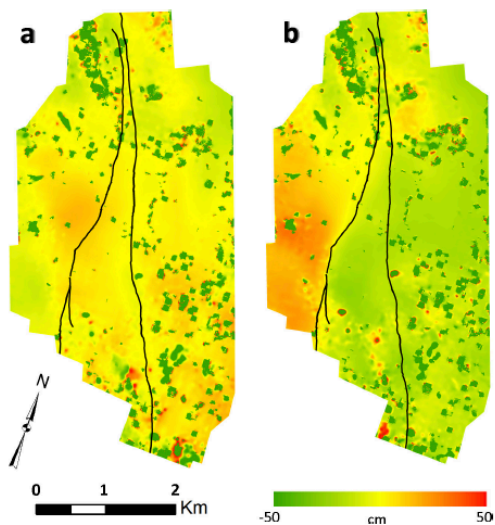


Fig. 6. Horizontal components of displacement field estimated with SfM data using ICP. (a) EW component. (b) NS component. Raw displacement estimates have been filtered using the NL-means filter. Black lines: field measured fault traces A and C [5], [50].

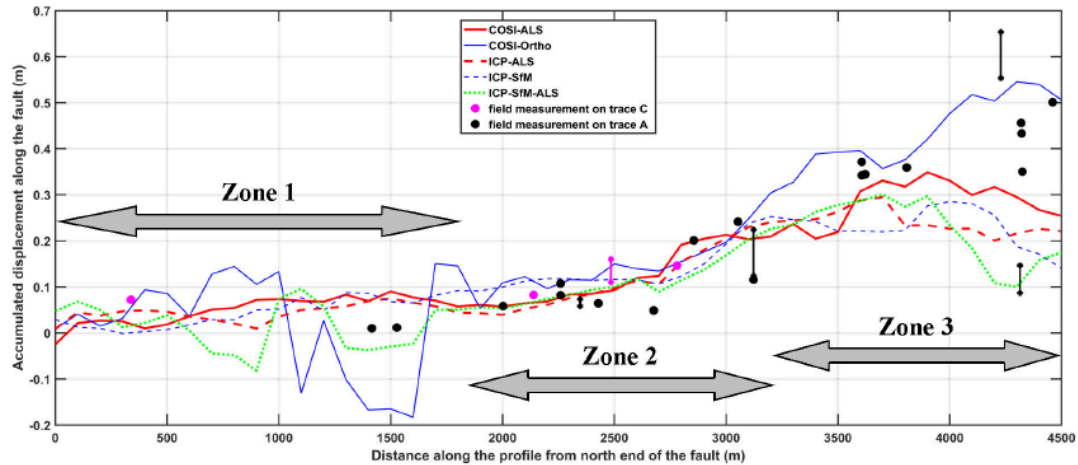


Fig. 8. Profiles showing accumulated along-the-fault displacement for the main ruptured fault. Red solid lines: COSI-ALS profile. Blue solid lines: COSI-ortho profile. Red dashed lines: ICP-ALS profile. Blue dashed lines: ICP-SfM profile. Green dotted line: ICP-SfM-ALS profile. Black dots: field measurements of offset features on fault trace A. Magenta dots: field measurements on fault trace C. Black and magenta solid lines: field measurements that were given as intervals. Specified zones correspond to the zones depicted on the top inset of Fig. 2.

Use of Planar Constraints To Improve Displacement Estimation Accuracy

The text in this section is a summary of the peer reviewed journal publication pertaining to this work:

Kusari, A., Glennie, C.L., Brooks, B.A., Ericksen, T.L., "Precise Registration of Laser Mapping Data by Planar Feature Extraction for Deformation Monitoring." IEEE Transactions on Geoscience and Remote Sensing, 2019, 57 (6), 3404-3422.

Although the ICP techniques applied to ALS datasets have been shown to reveal near-field surface deformation, they are only able to offer estimates with approximately decimeter scale accuracy. While the ICP algorithms work directly on the irregular point cloud dataset, the approach does not make any underlying assumptions about the scene that is depicted within the point cloud. While this methodology is very general, and applies to all situations, it does not take full advantage of any potential a-priori knowledge about the scene imaged in the point cloud. For example, in an urban environment, a number of the LiDAR returns will be measurements to buildings, rooftops, and other manmade objects. These manmade objects have known geometric properties, and these could be exploited to strengthen the solution for the spatial change between the point clouds, analogous to the use of persistent scatterer observations employed with differential radar observations (Hooper et al. 2004, Ferretti et al. 2004). We would therefore like to take advantage of known structure in the point clouds. Our initial attempt to improve the quality of the offset estimate obtained from the difference between two point clouds, examined constraining the LiDAR observations to planar surfaces, which are found in abundance in urban and suburban areas.

If we consider that we have two temporally spaced LiDAR point clouds, with an unknown spatial difference between them, we can then define the rigid body transformation that will align the two point clouds as:

$$\begin{bmatrix} X \\ Y \\ Z \end{bmatrix}_F = \begin{bmatrix} 1 & -\gamma & \beta \\ \gamma & 1 & -\alpha \\ -\beta & \alpha & 1 \end{bmatrix} \begin{bmatrix} X \\ Y \\ Z \end{bmatrix}_I + \begin{bmatrix} \Delta X \\ \Delta Y \\ \Delta Z \end{bmatrix} \quad (1)$$

where, $\vec{r}_F^T = [X \ Y \ Z]^T_F$ is the final transformed LiDAR point clouds, $\vec{r}_I^T = [X \ Y \ Z]^T_I$ are the initial offset LiDAR points, $\Delta X, \Delta Y, \Delta Z$ are the point cloud shifts, and α, β, γ are the angular offsets between the initial and final point cloud. Note that the formulation in equation 1 assumes that the angular offsets are small (less than 1°) which will always be the case when comparing two properly georeferenced point clouds referenced to the same geodetic datum. For each point observation, the optimized rigid body transformation parameters can be determined by a least squares solution given the following observational model (Skaloud and Lichti 2006):

$$\langle \vec{g}, \begin{bmatrix} \vec{r}_F \\ 1 \end{bmatrix} \rangle = 0 \quad (2)$$

where $\vec{g} = \langle g_1, g_2, g_3, g_4 \rangle$, are the parameters of the planar surface, that are used as constraints in the solution of the position and orientation offsets between the point clouds. Equation two applies to all n points in the final point cloud, constrained to all i observed planar surfaces, where $n \gg i$.

We first developed an automated algorithm for plane extraction, based on octree point cloud segmentation with subsequent region growing – the process is highlighted in Figure 1 below. This allowed an automatic identification of planar surfaces which could then be used for constraining the least squares solution.

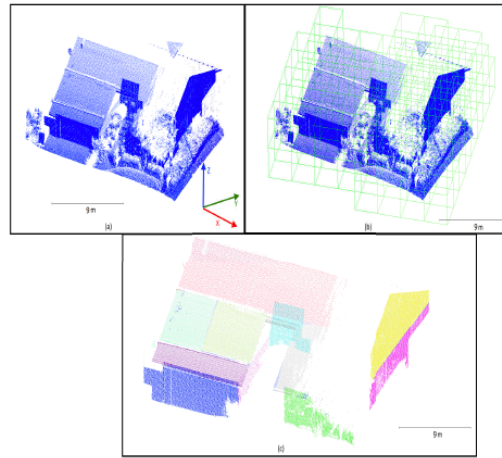


Fig. 1. Segmentation and planar region growing steps. (a) Original point cloud. (b) Octree division of the point cloud (green boxes representing nodes after third level of division). (c) Extracted planar surfaces colorized.

The analysis was carried out on both airborne laser scanning, and mobile laser scanning datasets collected before and after the August 24, 2014 Mw 6.0 Napa, California earthquake. The ALS data, similar to above allowed the determination of coseismic slip, since the data was collected pre- and post-event. The MLS datasets were both collected post event (approximately 8 and 38 days post earthquake), and therefore were examined to detect the presence of afterslip. The results from both the ALS and MLS datasets were compared with alinement array points located on the primary fault (Hudnut et al. 2014). A summary of the results are presented in the Tables below. The first table shows the estimate from ALS data (coseismic) compared to that measured at alinement array station NLOD. The second table shows results from MLS differences (afterslip) compared to the alinement array stations NLAR and NWIT.

TABLE 1
COMPARISON OF HORIZONTAL FAULT-PARALLEL ALS DISPLACEMENT ESTIMATE TO NLOD ALINEMENT ARRAY STATION ESTIMATE
FOR JUNE 2014-SEPTEMBER 2014 FOR NAPA FAULT IN THE BROWNS VALLEY NEIGHBORHOOD

Displacements	
ΔX (in m)	0.035 ± 0.0134
ΔY (in m)	0.0042 ± 0.0078
ΔHz (in m)	0.317 ± 0.0208
ΔHz (fault par) (in m)	0.313 ± 0.0192
ΔHz (NLOD) (in m)	0.309

TABLE 2
AFTERSLIP ESTIMATES FOR NAPA VALLEY FAULT AT SOUTH RURAL NAPA FROM MOBILE LASER SCANNING

Displacements	
ΔX (in m)	0.0105 ± 0.0027
ΔY (in m)	-0.0623 ± 0.0047
ΔZ (in m)	0.0161 ± 0.0089
ΔHz (in m)	0.0632
ΔHz (fault par) (in m)	0.0583
ΔHz (NLAR) (in m)	0.058
ΔHz (NWIT) (in m)	0.062

Overall, the constraints on planar surfaces suggest that sub cm estimates of displacement may be possible with lidar observations if we are able to constrain the lidar points to known surface observations. While the results are promising, there are also significant shortcomings in the analysis. First, and most obviously, it requires an urban environment where manmade structures provide the planar surfaces – this is obviously not possible in rural areas. For this initial proof of concept we also constrained the solution using all of the planar surfaces. This significantly limited the spatial resolution of the results. The constraint was necessary because single planes are sensitive to movement only along their normal direction – therefore an individual estimate of motion cannot be obtained by a single plane.

The text in this section is a summary of the peer reviewed journal publication currently in preparation entitled:

Zhu, X., Glennie, C.L., Brooks, B.A., Ericksen, T.L., "Automated Near-Field Deformation Estimates from Mobile Laser Scanning for the 2014 Mw 6.0 South Napa Earthquake." IEEE Transactions on Geoscience and Remote Sensing, (in preparation).

The planar constraints methodology described above is ideally suited to urban and suburban areas where a variety of man-made structures will provide a plethora of planar surfaces to use as persistent targets. However, in rural environments, such as that along the CSAF (creeping section of the San Andreas Fault), we cannot expect to find a sufficient number of man-made structures for displacement estimation. Fortunately, the mathematical model given above in equation (2) can be modified to provide constraints using mathematical representations of natural surfaces or other geometric primitives. These extensions to natural features and primitives have previously been used to calibrate airborne laser scanning instruments, e.g. (Filin 2003, Habib et al. 2005), and we adapted this methodology to provide estimations of displacement in rural areas.

We propose an automated change detection method using semantic primitives to reveal surface ruptures in the earthquake near field. Using mobile laser scanning (MLS), we acquired 3D point clouds representing the geometry of the earthquake rupture for the 2014 M6.0 South Napa earthquake (Brooks et al. 2017). Accumulated coseismic response is detected by monitoring deformation of linear primitives representing the geometry of vineyard rows which were straight prior to the earthquake. PointNet(Qi et al. 2017), a machine learning application specifically tailored to unorganized 3D point clouds is used to automatically segment point clouds and classify fence posts that are later modeled as cylindrical primitives – see Figure 1 below. Post seismic afterslip is detected by tracking these primitives between epochs of MLS data collected 7 and 34 days after the earthquake and it is shown that this method has the ability to detect subtle ground displacement in the near field. The detection results provide new observations of shallow fault slip with high-resolution and accuracy which are important for the study of rupture mechanisms for active faults. The proposed semantic primitives can be implemented in automated point cloud-based change detection and automatic point cloud segmentation.

Afterslip is estimated using the displacement of cylindrical primitives between two MLS surveys. To model the cylindrical primitives, representing posts on the scanned vineyard rows, point clouds need to first be segmented. In previous work, the segmentation was manually performed (DeLong et al. 2015)The process is complex and extremely time-consuming which limits the coverage of displacement estimates. Here we implement a deep neural network – PointNet to automatically segment MLS point clouds. The segmented point clouds are later

filtered using random sample consensus (RANSAC) and modeled as primitives using a least squares adjustment. Changes are derived by tracking the displacement of the cylindrical primitives between two epochs of MLS data.

PointNet proposed by (Qi et al. 2017) is a unique deep neural network that directly works on 3D point clouds. The network learns a set of optimization functions selecting informative points and aggregates the optimization results as global descriptors. Fully connected layers and symmetric max-pooling functions are implemented to handle the irregular format of point clouds.

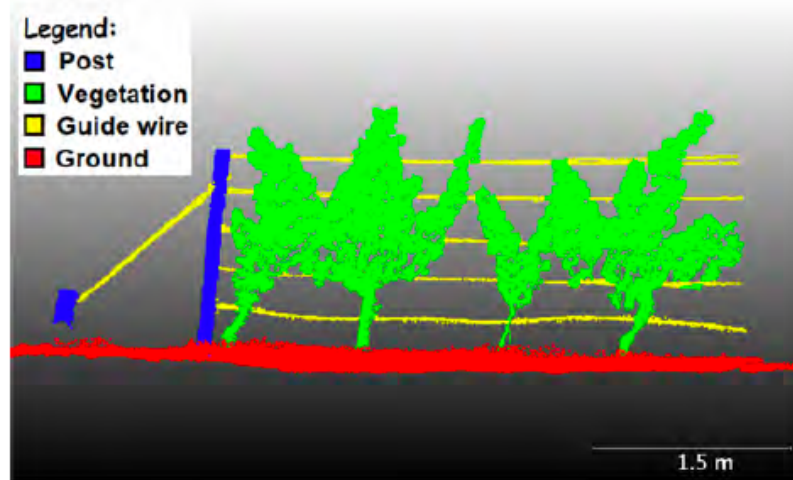


Figure 1: Segmentation example from a single vine row showing segmented MLS point cloud using PointNet.

For supervised learning on point clouds, we set up a vine row training set where 120 scanned vineyard row point clouds are manually labeled, consisting of 9 million labelled points in total. Every point within this set falls into one of four categories – fence posts, vegetation, guide wire, and ground. Random sampling from this training set generates over 40 thousand training samples, where each sample consists of 2048 points in a single vine row. The train-validation-test split is 7:1:2. Figure 1 shows a segmentation example where point clouds are automatically segmented into the four categories. After training, the network is capable of processing all 2600 scanned vineyard rows, which consists of over 300 million MLS laser points. The point clouds were automatically segmented into four categories and the fence posts were then extracted for cylindrical primitives modeling.

The segmented point clouds were modeled as cylindrical primitives and then pre- and post-deformed primitives were clustered by their locations. A Gauss-Helmert model is used for least squares fitting of cylindrical primitives:

$$g(l + e, p) = X^2 + Y^2 - r^2 = 0, \quad (1)$$

$$\text{where } \begin{bmatrix} X \\ Y \\ Z \end{bmatrix} = R_2(\phi)R_1(\omega) \begin{bmatrix} x_{obs.} \\ y_{obs.} \\ z_{obs.} - \bar{z}_{obs.} \end{bmatrix}, \quad (2)$$

$$R_1(\omega) = \begin{bmatrix} 1 & 0 & 0 \\ 0 & \cos \omega & \sin \omega \\ 0 & -\sin \omega & \cos \omega \end{bmatrix}, \quad (3)$$

$$R_2(\phi) = \begin{bmatrix} \cos \phi & 0 & -\sin \phi \\ 0 & 1 & 0 \\ \sin \phi & 0 & \cos \phi \end{bmatrix}, \quad (4)$$

where the inputs are MLS point clouds for a single post $[x_{obs}, y_{obs}, z_{obs}]^T$ with measurement uncertainties e . Point clouds are shifted and rotated so that a cylinder can be estimated at the center of each cloud with a vertical axis. The estimated parameters p are shift components (X, Y) , and rotation angles ω, ϕ for the x- and y-axis. The radius r of the cylinder is fixed at 5 inches (12.7 cm) for a typical anchor post.

Preliminary results from the cylindrical pole tracking are shown in Figure 9 below. Our initial analysis shows consistency between individual cylinders closely spaced at the ~cm level.

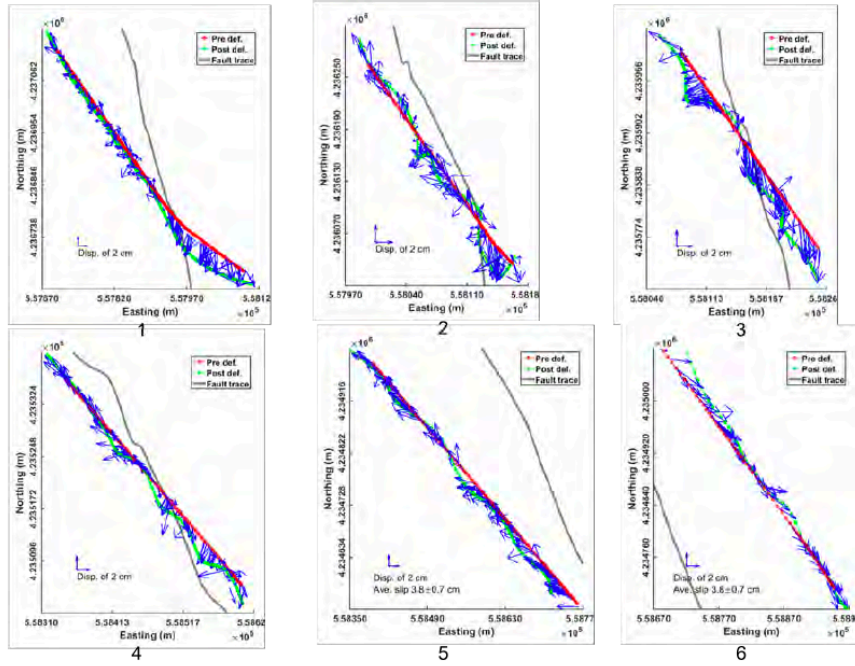


Fig. 9: Postseismic afterslip patterns detected for the six cases numbered in figure 7 (top: cases 1-3, bottom: cases 4-6). Regression lines show how linear features deformed by fault crossing with red and green lines representing pre- and post-deformation locations.

Publications and Presentations Related to This Work

Refereed Journal Publications

1. Nevitt, J.M., B.A. Brooks, R.D. Catchings, M.R. Goldman, T.L. Ericksen, and C.L. Glennie. "Mechanics of Near-Field Deformation During Co- and Post-Seismic Shallow Fault Slip." *Nature Scientific Reports*, 10, 2020: 5031. doi: 10.1038/s41598-020-61400-9.
2. Kusari, A., Glennie, C.L., Brooks, B.A., Ericksen, T.L., "Precise Registration of Laser Mapping Data by Planar Feature Extraction for Deformation Monitoring." *IEEE Transactions on Geoscience and Remote Sensing*, 2019, 57 (6), 3404-3422.
3. Ekhtari, N., and Glennie, C.L., "High-Resolution Mapping of Near-Field Deformation With Airborne Earth Observation Data, a Comparison Study," *IEEE Transactions on Geoscience and Remote Sensing*, 2018, 56(3), 1598-1614.
4. Brooks, B.A., Minson, S.E., Glennie, C.L., Nevitt, J.M., Dawson, T., Rubin, R., Ericksen, T.L., Lockner, D., Hudnut, K.W., Langenheim, V., Lutz, A., Mareschal, M., Murray, J., Schwartz, D., Zaccane, D., "Buried Shallow Fault Slip from the South Napa Earthquake Revealed by Near-Field Geodesy," *Science Advances*, 2017 3(7), e1700525.

Presentations/Posters

1. Nevitt, J.M., Brooks, B.A., Lockner, D.A., Morrow, C.A., Catchings, R., Goldman, M., Moore, D.E., Melosh, B.L., Criley, C., Ericksen, T.L. and Glennie, C.L., 2019. Fault Behavior and Surface Deformation Linked to Shallow Mechanical Properties during the 2014 M6.0 South Napa Earthquake. AGU Fall Meeting, San Francisco, CA, December 2019, T22D-06.
2. Hartzell, P.J. and Glennie, C.L., 2019. Rigorous Error Propagation for Topographic Displacements Derived from Image Correlation. AGU Fall Meeting, San Francisco, CA, Dec. 2019, NH14A-08.
3. Zhu, X., Glennie, C.L. and Brooks, B.A., Automated Change Detection Using Cylindrical Primitives Generated from a Deep Neural Network. AGU Fall Meeting, San Francisco, CA, December 2019, NH14A-05.
4. Nevitt, J.M., Brooks, B.A., Lockner, D.A., Melosh, B.L., Catchings, R., Goldman, M., Morrow, C.A., Moore, D.E., Criley, C., Ericksen, T.L. and Glennie, C.L., A Multidisciplinary Investigation of Fault-Driven Plastic Deformation in Earth's Shallowest Crust. AGU Fall Meeting, San Francisco, CA, December 2019, MR44A-01.
5. Brooks, B.A., et al., "Shallow Fault Slip and Near-fault Deformation on the Creeping Section of the San Andreas Fault," AGU Fall Meeting, Washington, DC, December 2018, T42D-06.
6. Nevitt, J., Brooks, B. A., Catchings, R., Goldman, M., Criley, C., Chan, J. H., Glennie, C. L., Ericksen, T. L., Madugo, C. M., "Co- and post-seismic shallow fault physics from near-field geodesy, seismic tomography, and mechanical modeling," AGU Fall Meeting, New Orleans, LA, December 2017, G43C-03
7. Glennie, C., Kusari, A., Brooks, B.A., Ericksen, T.E., "Automated Near-Field Displacement Estimates from Mobile Laser Scanning – Case Study for the Mw 6.0 August 24, 2014 Napa Earthquake," AGU Fall Meeting, San Francisco, CA, December 2016, T32B-04.
8. Nevitt, J., Brooks, B.A., Minson, S.A., Lockner, D.A., Moore, D.E., Ericksen, T.E., Hudnut, K.W., Glennie, C.L., Madugo, C.M., "Effects of Elastoplastic Material Properties on Shallow Fault Slip and Surface Displacement Fields," San Francisco, CA, December 2016, T22B-07.
9. Lyda, A., Zhang, X., Glennie, C, Hudnut, K., and B. Brooks, "Airborne light detection and ranging (lidar) derived deformation from the Mw 6.0 24 August 2014 South Napa earthquake estimated by two and three dimensional point cloud change detection techniques," ISPRS General Assembly, Prague, Czech Republic, July 12-19, 2016.

References

- Besl, P. J. & N. D. McKay (1992) A method for registration of 3-D shapes. *Pattern Analysis and Machine Intelligence, IEEE Transactions on*, 14, 239-256.
- Brooks, B. A., S. E. Minson, C. L. Glennie, J. M. Nevitt, T. Dawson, R. Rubin, T. L. Ericksen, D. Lockner, K. Hudnut, V. Langenheim, A. Lutz, M. Mareschal, J. Murray, D. Schwartz & D. Zaccane (2017) Buried shallow fault slip from the South Napa earthquake revealed by near-field geodesy. *Science Advances*, 3.
- DeLong, S. B., J. J. Lienkaemper, A. J. Pickering & N. N. Avdievitch (2015) Rates and patterns of surface deformation from laser scanning following the South Napa earthquake, California. *Geosphere*, 11, 2015-2030.
- Ferretti, A., F. Novali, R. Bürgmann, G. Hilley & C. Prati (2004) InSAR permanent scatterer analysis reveals ups and downs in San Francisco Bay Area. *Eos, Transactions American Geophysical Union*, 85, 317-324.
- Filin, S. (2003) Recovery of systematic biases in laser altimetry data using natural surfaces. *Photogrammetric Engineering & Remote Sensing*, 69, 1235-1242.
- Glennie, C. L., A. Hinojosa-Corona, E. Nissen, A. Kusari, M. E. Oskin, J. R. Arrowsmith & A. Borsa (2014) Optimization of legacy lidar data sets for measuring near-field earthquake displacements. *Geophysical Research Letters*, 41, 2014GL059919.
- Habib, A., M. Ghanma, M. Morgan & R. Al-Ruzouq (2005) Photogrammetric and LiDAR data registration using linear features. *Photogrammetric Engineering & Remote Sensing*, 71, 699-707.
- Hooper, A., H. Zebker, P. Segall & B. Kampes (2004) A new method for measuring deformation on volcanoes and other natural terrains using InSAR persistent scatterers. *Geophysical Research Letters*, 31.
- Hudnut, K. W., T. M. Brocher, C. S. Prentice, J. Boatwright, B. A. Brooks, B. Aagaard, J. Blair, J. Fletcher, J. Erdem, C. Wicks, J. Murray, F. Pollitz, J. Langbein, J. Svarc, D. Schwartz, D. Ponti, S. Hecker, S. DeLong, C. Rosa, B. Jones, R. Lamb, A. Rosinski, T. McCrink, T. Dawson, G. Seitz, R. Rubin, C. Glennie, D. Hauser, T. Ericksen, D. Mardock, D. Hoirup & J. Bray. 2014. Key Recovery Factors for the August 24, 2014, South Napa Earthquake. In *US Geological Survey Open-File Report*, 51.
- Leprince, S., S. Barbot, F. Ayoub & J. P. Avouac (2007) Automatic and Precise Orthorectification, Coregistration, and Subpixel Correlation of Satellite Images, Application to Ground Deformation Measurements. *Geoscience and Remote Sensing, IEEE Transactions on*, 45, 1529-1558.
- Qi, C. R., H. Su, K. Mo & L. J. Guibas. 2017. Pointnet: Deep learning on point sets for 3d classification and segmentation. In *Proceedings of the IEEE conference on computer vision and pattern recognition*, 652-660.
- Skaloud, J. & D. Lichti (2006) Rigorous approach to bore-sight self-calibration in airborne laser scanning. *Isprs Journal of Photogrammetry and Remote Sensing*, 61, 47-59.
- Zhang, X., C. Glennie & A. Kusari (2015a) Change Detection From Differential Airborne LiDAR Using a Weighted Anisotropic Iterative Closest Point Algorithm. *Selected Topics in Applied Earth Observations and Remote Sensing, IEEE Journal of*, PP, 1-9.
- (2015b) Change Detection From Differential Airborne LiDAR Using a Weighted Anisotropic Iterative Closest Point Algorithm. *Selected Topics in Applied Earth Observations and Remote Sensing, IEEE Journal of*, 8, 3338-3346.